

RESEARCH ARTICLE

Moist convective scaling: Insights from an idealised model

Lokahith Agasthya¹  | Caroline Muller¹  | Mathis Cheve^{1,2}¹Institute of Science and Technology
Austria, Klosterneuburg, Austria²École Normale Supérieure de Lyon,
Lyon, France**Correspondence**Lokahith Agasthya, Institute of Science
and Technology Austria, Am Campus 1,
3400 Klosterneuburg, Austria.
Email: lnagasthya@gmail.com**Funding information**H2020 Marie Skłodowska-Curie Actions,
Grant/Award Number: 101034413; H2020
European Research Council,
Grant/Award Number: 805041**Abstract**

The response of clouds and moist-convective processes to heat loss to space by long-wave radiative cooling is an important feedback in the Earth's atmosphere. It is known that moist convection increases roughly in equilibrium with radiative cooling, an assumption often made in simplified models of the tropical atmosphere. In this study, we use an idealised two-dimensional model of the atmosphere introduced by Vallis et. al. and incorporate a bulk-cooling term, which is an idealisation of radiative cooling in the atmosphere. We comment briefly on the static stability of the system to dry and moist convection and characterise its moist convective response to changes in the bulk cooling. We find that, while the clear-sky regions of the model respond directly to the change in the cooling term, the regions dominated by moist convective plumes are insensitive to changes in cooling. Similar to previous findings from cloud-resolving models, we too find in our idealised setting that the majority of the increase in convection occurs via an increase in the areal coverage of convection, rather than its intensity. We argue that these small-scale convective processes are an upper bound on how quickly convective intensity can change to stay in equilibrium with radiative cooling.

KEYWORDS

moist convection, radiative cooling, Rayleigh-Bénard

1 | INTRODUCTION

The cooling of the atmosphere by radiative heat loss to space through outgoing long-wave radiation is one of the most important feedbacks on global climate. Radiative cooling occurs through a highly interactive, non-linear mechanism with strong vertical and latitudinal variations. Locally, it is strongly dependent on temperature, water-vapour content, cloud height and type, the nature of aerosols, partition of water into solid (ice) and liquid phases, and several other atmospheric chemical and physical properties. Globally, it is known that the

Earth is roughly in thermodynamic equilibrium, with the annualised, global mean value of outgoing radiation measured to be $\sim 1.5\text{K} \cdot \text{d}^{-1}$ (Jeevanjee & Fueglistaler, 2020).

Simplified models of the tropical atmosphere often make the assumption of radiative convective equilibrium (RCE) the atmosphere is assumed to be in a quasi-equilibrium where moist convection and radiative cooling balance each other over long enough time-scales through convective adjustment (Manabe & Strickler, 1964; Tompkins & Craig, 1998). Moist convection is a mechanism by which heat from the Earth's surface (heated directly by incoming solar short-wave radiation) is

This is an open access article under the terms of the [Creative Commons Attribution](https://creativecommons.org/licenses/by/4.0/) License, which permits use, distribution and reproduction in any medium, provided the original work is properly cited.

© 2024 The Author(s). *Quarterly Journal of the Royal Meteorological Society* published by John Wiley & Sons Ltd on behalf of Royal Meteorological Society.

transported upward in the atmosphere in the form of both sensible heat, which is the direct transport of heat by advection, and latent heat, through the transport of water vapour, which condenses aloft in the atmosphere. In RCE, these surface fluxes heating the atmosphere are in equilibrium with radiative cooling.

While global climate models are used to understand projected changes in climate and the feedback from various processes on the climate (Sherwood *et al.*, 2015, 2020), recently cloud-resolving models (CRMs) have become an important tool to investigate the tropical atmosphere at smaller scale with higher resolution modelling (Khairoutdinov & Randall, 2003). This approach has gained prominence due to the fact that most GCMs rely on convective parametrisations (Arakawa & Wu, 2013) and are typically not run at high enough resolutions to resolve convection due to the large computational requirements, though recent advancements have made high-resolution GCMs without convective parametrisations a reality (Stevens *et al.*, 2019). Clouds associated with moist convection are known to be a large source of uncertainty in global climate models (Bony & Dufresne, 2005; Klein *et al.*, 2017; Zelinka *et al.*, 2022).

CRMs are typically run over smaller, often idealised domains of the order of a few hundred to a few thousand kilometres in the horizontal direction. CRMs have proved to be extremely successful at providing key and valuable insights into the processes of moist convection (Stauffer & Wing, 2022; Wing & Emanuel, 2014) and also the possible changes in tropical climate with a changing climate characterised by higher surface temperatures (Muller *et al.*, 2011). These idealisations allow for the examination of the role of various feedbacks from processes involved in moist convection through sensitivity experiments that are simple to implement.

However, CRMs usually involve solving equations for a large number of prognostic variables and model parameters, since they parametrise several small-scale processes in great detail, in particular subgrid fluxes and cloud microphysics, making interpretation of results difficult. It is often found that the choice of such parametrisation can have a significant impact on the resulting dynamics (Parodi & Emanuel, 2009; Singh & O’Gorman, 2014). In this situation, more theoretical and “blank-slate” simplified studies of moist convection with a few parameters and highly idealised representation of small-scale processes are valuable. Such an approach can lead to a simplified but still qualitatively accurate representation of convection. In line with this approach are recent studies by Pauluis and Schumacher (2010), Hernandez-Duenas *et al.* (2013), and Vallis *et al.* (2019), among others. Here the idea is to represent only the main processes that drive the dynamics of moist convection, that is, the release or absorption of

heat by the change of phases in water. This makes their implementation, as well as interpretation, much more straightforward. Another advantage of simplified models is the vast existing literature on idealised models of dry convection. Rayleigh–Bénard convection is among the best characterised and well-studied natural models (Ahlers *et al.*, 2009). As remarked by Vallis *et al.* (2019), (henceforth Val2019), there is very little overlap between the study of Rayleigh–Bénard convection and theoretical studies of atmospheric moist convection, particularly of deep convection (i.e., convective clouds that span the whole troposphere).

In the current study, we adopt a simple model of moist convection that shares a number of features of Rayleigh–Bénard convection, termed “Rainy–Bénard convection” by Vallis *et al.* (2019). The Rainy–Bénard model consists of a layer of incompressible, Boussinesq fluid with the top and bottom of the layer held at constant temperature (as in conventional Rayleigh–Bénard convection), along with fixed moisture boundary conditions. Virtual effects of water are neglected and water vapour is assumed to condense and precipitate instantaneously upon reaching saturation. The saturation specific humidity is assumed to follow a simple exponential dependence on temperature. We take forward the model of Rainy–Bénard convection and add a uniform, bulk cooling term to mimic atmospheric radiative cooling. We set realistic boundary conditions and fluid parameters, within the limit of available computational resources, and vary the single value of radiative cooling. We describe and quantify the resulting dynamics, comparing it with known results on the variation of radiative cooling in CRMs.

Notably, Robe and Emanuel (1996) found that, as the radiative cooling (constant in their idealised CRM experiments) was increased, the convective mass flux showed a roughly linear increase in response. This is expected theoretically, as the subsidence velocity outside clouds is expected to increase proportionally to the radiative cooling (Robe & Emanuel, 1996; Shutts & Gray, 1999). By mass conservation, this implies a similar increase in the upward mass flux in clouds. However, there are no theoretical constraints on how this increased cloud mass flux is reached. This increase could come from either increased mean vertical velocity in clouds or increased cloud area. The scaling of mass flux in clouds is central to the problem of cumulus parametrisation as originally formulated by Arakawa and Schubert (1974).

Robe and Emanuel (1996)’s numerical simulations showed that most of the convective mass flux increase with strong cooling is due to increased cloud area, while vertical velocities in clouds remain approximately constant. Additional evidence for this scaling has also been seen in numerical simulations of Shutts and Gray (1999).

and Parodi and Emanuel (2009). Observational data (see table 1 of Davies *et al.* (2013).) found a high correlation between total precipitation and precipitation area (closely related to cloud coverage), while finding a low correlation between total precipitation and precipitation intensity (closely related to updraft strength), strongly suggesting that, in a convecting atmosphere, it is chiefly area rather than intensity of convection that varies in response to the large-scale forcing. The evidence for such a scaling is reviewed in Yano and Plant (2012)., where the dynamic implications of the independence of vertical velocity to varying large-scale forcing while convective area increases is also studied.

Here, we first investigate whether our simple model of moist convection correctly captures this behaviour found in more complex CRM simulations. Second, we explore whether this can be understood using simple scalings for the vertical velocity in clouds. Importantly, we argue that the small changes in vertical velocities are due to small-scale convective processes, which limit their ability to increase strongly in response to the enhanced radiative cooling.

The rest of the article is organised as follows. Section 2 describes the model and the parameters chosen for the numerical experiments, along with a quick summary on the large-scale balances that are expected from the model equations. Section 3 summarises the results of our numerical simulations. Section 3.1 briefly discusses the static stability for the chosen fluid configuration in the presence and absence of moisture and radiative cooling. This is followed by a detailed description of the behaviour of the system when varying the bulk cooling in Section 3.2. Chiefly, in Section 3.2.1 we examine the scaling of the area fraction of the domain undergoing moist convection, the vertical velocity, and the convective mass flux with the bulk-radiative cooling. In Sections 3.2.2–3.2.4, we propose and examine predictions for the scaling of vertical velocity extremes based on CAPE, buoyancy integrals, and cloud-plume models. In Section 3.2.5, we compare the velocity statistics for the moist model with the corresponding dry convective model. We conclude the article in Section 4 with a discussion of our results and avenues for future work.

2 | METHODOLOGY

2.1 | Model and equations

Our starting point is the Rainy–Bénard equations of Val2019, with an additional bulk cooling term $-R$ in the temperature equation, which represents the radiative cooling to space, constant in space and time in our idealised

system. We write the equations explicitly in terms of the temperature for a two-dimensional (x, z) Boussinesq fluid with the buoyancy force proportional to the coefficient of thermal expansion β . The equations for the velocity $\mathbf{u} = (u, w)$, the temperature T , and the specific humidity q (mass of water vapour per unit mass of air) are given by

$$\nabla \cdot \mathbf{u} = 0, \quad (1)$$

$$\partial_t \mathbf{u} + (\mathbf{u} \cdot \nabla) \mathbf{u} = -\nabla p + \nu \nabla^2 \mathbf{u} - \beta T \mathbf{g}, \quad (2)$$

$$\partial_t T + \mathbf{u} \cdot \nabla T + \Gamma_d w = \kappa \nabla^2 T + L_v \tau^{-1} (q - q_s)_+ - R, \quad (3)$$

$$\partial_t q + \mathbf{u} \cdot \nabla q = \kappa_q \nabla^2 q - \tau^{-1} (q - q_s)_+. \quad (4)$$

Here, Γ_d is the dry-adiabatic lapse rate g/c_p with potential temperature θ defined as $\theta \equiv T + \Gamma_d z$, $\mathbf{g} = (0, g)$ is the amplitude of the acceleration due to gravity, c_p is the specific heat capacity of dry air at constant pressure, and q_s is the saturation specific humidity of water vapour, which is a function of temperature only in our case. Further, L_v is the latent heat of condensation of water divided by c_p , κ and κ_q are the diffusivities of heat and moisture, respectively, and ν is the kinematic viscosity. a_+ denotes the positive part of a , where $a_+ = 0$ when a is negative and $a_+ = a$ when a is positive. τ is a time-scale of condensation, which is set to be very small, so that condensation is almost instantaneous whenever the specific humidity of water vapour $q > q_s$. Note that condensates are assumed to precipitate instantaneously, so there are no suspended condensates (no sustained clouds) in our simulations.

In this system, q is assumed always to be small, such that virtual effects arising from the presence of water vapour are neglected. Thus, the changes in density and heat capacity of air due to water vapour are not included in the model. The simplified Clausius–Clapeyron equation for the saturation specific humidity of water vapour in the model is given by (Vallis *et al.*, 2019)

$$q_s(T) = q_0 \exp \alpha(T - T_0), \quad (5)$$

where $T_0 = 300\text{K}$, with q_0 being the saturation specific humidity at $T = T_0$.

It remains to specify the boundary conditions for the system. The domain is periodic in the horizontal direction. The temperature and specific humidity are kept constant at the top and bottom boundaries while the fluid is held motionless. The values are

$$\mathbf{u}(z = 0) = \mathbf{u}(z = 10 \text{ km}) = \mathbf{0}; \quad (6)$$

$$T(z = 0) = 300 \text{ K}; \quad (7)$$

$$T(z = 10 \text{ km}) = 230 \text{ K}; \quad (8)$$

$$q(z = 0) = 0.8q_s(300 \text{ K}) = 0.02 \text{ kg} \cdot \text{kg}^{-1}; \quad (9)$$

$$q(z = 10 \text{ km}) = 0.1q_s(230 \text{ K}) = 5.26 \times 10^{-5} \text{ kg} \cdot \text{kg}^{-1}. \quad (10)$$

The bottom and top surfaces are held at constant relative humidities of 80% and 10% respectively. Henceforth, we use T_{bot} and q_{bot} to denote the set temperature and specific humidity at the lower boundary and T_{top} and q_{top} to denote the same quantities at the top boundary. The temperature difference between the lower surface and the upper surface is 70 K, which is smaller than the “dry adiabatic” value 100 K; the underlying dry system is thus stable to dry convection. Other possible boundary conditions include various combinations of prescribed constant heat flux or constant moisture flux. We found that using fixed flux for temperature or moisture often led to a drift in these values until the boundary became supersaturated. In the interest of continuity from Val2019, simplicity in understanding the underlying stability, and to avoid any numerical issues at the boundary, we retain the fixed-temperature boundary conditions.

The equations are written here in terms of the temperature T rather than buoyancy b (as in Val2019) and with changes in density expressed through change in T assumed to be proportional to the expansion coefficient β . The choice of using temperature is to help readers to make direct comparisons with dimensional, atmospheric values. Dynamically, these equations are identical to the equations in Val2019, except for the bulk-cooling term, which is the main focus of our study.

We solve the adimensionalised equations (Equations 1–4) with length, time, and temperature normalised by 1 km, 1 hr, and 1 K respectively. The equations are solved in Python using the initial value problem (IVP) command from the Dedalus package (Burns *et al.*, 2020). Dedalus

provides an open-source framework for solving differential equations by spectral decomposition. The equations are solved by decomposition into spectral bases, using Fourier bases for the horizontal direction and Chebyshev polynomial bases for the vertical direction. Dedalus allows the user to simply input differential equations as strings, allowing for quick and easy code development.

It is possible here to define length, time, moisture, and temperature scales based on the model parameters and find non-dimensional parameters (such as the Rayleigh number) that describe the dynamics of the system fully, as is done in previous studies of idealised moist convection (Pauluis & Schumacher, 2010; Vallis *et al.*, 2019). We note here that the stability and scaling of the dynamical response of the model itself to varying model parameters is a problem of great interest to a wide section of researchers. However, the current study is focused on understanding the scaling of moist convection in the atmosphere using the idealised model rather than a study of the model itself. We include a short note on the non-dimensionalisation of the equations in Appendix A to enable comparison with previous direct numerical simulation studies for the interested reader.

Table 1 summarises the parameters and scales used in the simulations. The simulation corresponds to a domain 100km wide and 10km high. Values of temperature, specific humidity, and saturation specific humidity are realistic. We set large values for the dissipation constants κ , ν , and κ_q , while keeping their ratios realistic. That is, the non-dimensional constants of viscous forces, the Prandtl number $\text{Pr} = \nu/\kappa$ and the water-vapour Prandtl

TABLE 1 Parameters used for simulations of moist internally cooled convection with varying R , solved using Dedalus on a 100km \times 10km domain and a 2048 \times 256 grid. We set $T_{\text{bot}} = 300\text{K}$, $T_{\text{top}} = 230\text{K}$, $q_{\text{bot}} = 0.8q_s(T_{\text{bot}})$, and $q_{\text{top}} = 0.1q_s(T_{\text{top}})$. In other simulations, κ , βg , and the boundary conditions are varied and the chosen parameters are stated clearly in the text describing the results.

Quantity	Value in simulation	Physical units	Typical atmospheric value
Length	1	1 km	–
Time	1	1 h	–
Temperature	1	1 K	–
κ	0.004	$1.1\text{m}^2 \cdot \text{s}^{-1}$	$\sim 2 \times 10^{-5}\text{m}^2 \cdot \text{s}^{-1}$
ν	0.0028	$0.77\text{m}^2 \cdot \text{s}^{-1}$	$\sim 1.5 \times 10^{-5}\text{m}^2 \cdot \text{s}^{-1}$
κ_q	0.0052	$1.43\text{m}^2 \cdot \text{s}^{-1}$	$\sim 2.6 \times 10^{-5}\text{m}^2 \cdot \text{s}^{-1}$
βg	1	$7.5 \times 10^{-5}\text{m} \cdot \text{s}^{-2} \cdot \text{K}^{-1}$	$\sim 0.03\text{m} \cdot \text{s}^{-2} \cdot \text{K}^{-1}$
$\Gamma_d = g/c_p$	10	$10\text{K} \cdot \text{km}^{-1}$	$10\text{K} \cdot \text{km}^{-1}$
L_v/c_p	2500	2500 K	$\sim 2500\text{K}$
q_0	0.025	$0.025\text{kg} \cdot \text{kg}^{-1}$	$0.025\text{kg} \cdot \text{kg}^{-1}$
α	0.05516	0.05516K^{-1}	$\sim 0.055\text{K}^{-1}$
R	[0 – 0.3]	$[0 - 7.2]\text{K} \cdot \text{d}^{-1}$	$[1 - 2]\text{K} \cdot \text{d}^{-1}$

number $Pr_q = \kappa_q/\kappa$ are both set to their dry-air values of 0.7 and 1.3 respectively. Thus, we are simulating an atmosphere where the viscous, dissipative forces are far larger in magnitude and the buoyancy force (βg) is weaker than in reality. The Rayleigh number Ra is 6.25×10^9 , where the definition of the Rayleigh number follows the one in Val2019 (see their equation 4.15a; more details can be found in Appendix A). Increasing the Rayleigh number by decreasing the dissipation constants would require a far higher resolution numerical grid and much greater computational resources to have a well-resolved energy cascade in the absence of any subgrid-scale parametrisations.

The time-scale of condensation τ is set small enough to ensure that large regions of supersaturation (i.e., with relative humidity larger than 100%) do not develop anywhere in the domain, with the maximum relative humidity attained staying below 1.02. This ensures that all simulations are in the regime of instantaneous condensation and precipitation. For the largest value of $R = 7.2 \text{ K} \cdot \text{d}^{-1}$, this corresponds to $\tau = 0.36 \text{ s}$ or 1×10^{-4} in simulation units. For smaller values of R , τ is increased appropriately to have faster simulation wall time. We have checked via shorter runs that the precise value of τ chosen does not affect the main results as long as the simulation remains in the regime of instantaneous condensation.

2.2 | Large-scale energy balance

For a system in thermal equilibrium, the sum of the sensible heat flux and the latent heat flux into the system from the boundaries must balance the net radiative cooling in the domain. This is expressed as

$$\frac{\kappa}{L_z} \left(\partial_z \bar{T} \Big|_{z=L_z} - \partial_z \bar{T} \Big|_{z=0} \right) + L_v \frac{\kappa_q}{L_z} \left(\partial_z \bar{q} \Big|_{z=L_z} - \partial_z \bar{q} \Big|_{z=0} \right) = R. \quad (11)$$

The above equation is derived by first summing Equation (3) and Equation (4) multiplied by L_v and then considering the domain average of the resulting equation in the steady state (overbars denote horizontal and time averages). Time and horizontal derivatives vanish, due to the steady-state condition and the periodic boundary conditions respectively. Since $w = 0$ at the top and bottom boundaries, the domain average depends only on the vertical gradients of the temperature and specific humidity evaluated at these boundaries.

The four terms on the left-hand side (LHS) of Equation (11) are the sensible heat flux into the domain from the top and bottom boundaries and the latent heat flux from the top and bottom boundaries, respectively. The four terms summing up to R is a check that the simulations are in

thermal equilibrium. The heightwise heat transfer can be deduced by considering only the horizontal average of the sum of Equation (3) and L_v times Equation (4). An integration in the variable z between z and L_z gives

$$\overline{w(T + L_v q)} - \partial_z (\kappa \bar{T} + L_v \kappa_q \bar{q}) = R(L_z - z) + C_0. \quad (12)$$

Here again, the overbar indicates the time and horizontal average at a given height z and C_0 is a constant of integration equal to (minus) the sum of the outgoing latent and sensible heat flux at the top boundary ($C_0 = -\partial_z (\kappa \bar{T} + L_v \kappa_q \bar{q}) \Big|_{z=L_z}$). The first two terms on the LHS represent the convective transport of sensible heat and latent heat, respectively, while the latter two terms represent the conductive transport of sensible heat and latent heat. The sum of these is thus a straight line in z with slope $-R$. The convective transport terms show large variations in time, and Equation (12) is not satisfied at any instantaneous time. Statistically, however, Equation (12) is satisfied in our simulations, which is essential to ensure that the statistics measured in the study represent the true long-term, steady-state behaviour and not a transient solution.

3 | RESULTS

3.1 | Conditional stability

For the temperature boundary conditions chosen, the dry system ($q = 0$) with no radiative cooling ($R = 0$) is stable to small perturbations, as the steady-state solution ($\mathbf{u} = 0$, $\kappa \nabla^2 T = 0 \Rightarrow T(z) = (T_{\text{top}} - T_{\text{bot}})z/L_z + T_{\text{bot}}$) has a linear temperature profile with a gradient of $7 \text{ K} \cdot \text{km}^{-1}$ that is less steep than the adiabatic lapse rate of $10 \text{ K} \cdot \text{km}^{-1}$. In the presence of moisture, the static stability is determined by a combination of the moisture and temperature boundary conditions. While the steady-state solution ($q(z) = (q_{\text{top}} - q_{\text{bot}})z/L_z + q_{\text{bot}}$) is given by a linear decrease of q with height, q_s decreases much faster (exponentially) with height, with condensation likely to trigger convection in the system. The steady-state solution where condensation occurs without convection and the latent heat is balanced exclusively by thermal dissipation is discussed by Val2019 (section 5, “The drizzle solution”). When R is non-zero, the steady-state solution depends on R —the variation of this solution with R and its linear stability are not considered in this study.

For the chosen q_{bot} and q_{top} , the system is unstable and shows moist convection even with $R = 0$. The convection is not steady in time—instead, it is interspersed by long time periods during which the fluid is quiescent

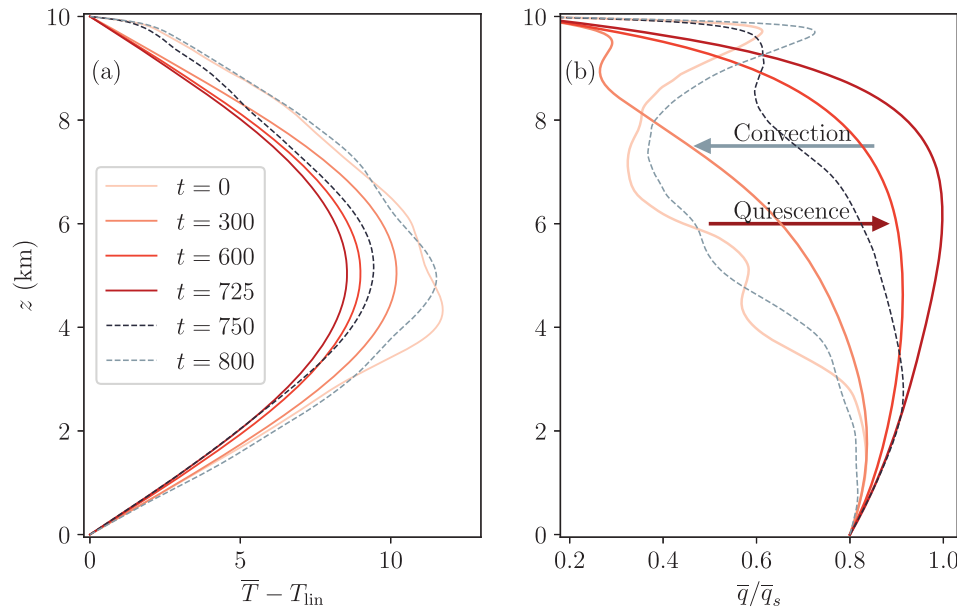


FIGURE 1 The temperature and relative humidity profiles for the moist simulations with $R = 0$. (a) The anomaly of the horizontally averaged temperature profile \bar{T} with respect to the linear temperature profile $T_{\text{lin}} = (T_{\text{top}} - T_{\text{bot}})z/L_z + T_{\text{bot}}$ for different times. (b) Average relative humidity profile \bar{q}/\bar{q}_s for different times. Time is in simulation units.

and the temperature gradually decreases while the quantity of moisture in the domain increases, both quantities relaxing towards a linear profile. Thus, the relative humidity q/q_s increases through both an increase in q and a decrease in q_s . When the domain reaches saturation in some regions, it leads to local condensation and convection, which quickly becomes space-filling. Rapid convective adjustment brings the system back to a quiescent warm, dry state through condensation and latent heating and the process repeats cyclically. Figure 1, showing the average temperature and relative humidity profiles at different times, summarises this behaviour. Initially, at $t = 0$ (light red, solid curve), the temperature is warm in the bulk and the relative humidity is well below 1 everywhere. The temperature slowly shifts towards the linear profile (darker shades of red) until around $t = 725$, where q/q_s between $z \sim 6$ and $z \sim 8$ is very close to 1. Condensation occurs here, heating up the system and causing the temperature to once again gain a strong positive anomaly with respect to the linear profile (blue dashed curves), with the domain becoming drier. At $t = 800$ (light, blue dashed curve), the system is again where it was at $t = 0$ (light, red dashed curve) and returns to a quiescent state. Supplementary Movie 1 in the Supporting Information shows an animation of the relative-humidity field (top panel) and the profiles of T (bottom left panel), q , and q_s (bottom right panel).

For $R > 0$, the dry steady-state solution ($\mathbf{u} = \mathbf{0}$) is given by a parabolic temperature profile in z such that $\partial_z^2 T = R/\kappa$, which can be solved analytically for the fixed-temperature boundary conditions. The static stability of the solution can be ascertained by checking whether

$\partial_z T < -10 \text{ K} \cdot \text{km}^{-1}$ everywhere. In our case, static stability holds everywhere for $R < 5.76 \times 10^{-2} \text{ K} \cdot \text{d}^{-1}$. Thus, even a small magnitude of radiative cooling alone destabilises the fluid layer and leads to dry convection. The precise small value of R for which the moist convection changes from intermittent to continuous has not been explored in this study. Instead, we focus on the response of moist convection to varying radiative cooling rates, which we discuss next.

3.2 | Varying radiative cooling

In the rest of the article, we focus on the behaviour of the system for five non-zero values of radiative cooling, $R = 0.72, 1.5, 1.95, 3.6, \text{ and } 7.2 \text{ K} \cdot \text{d}^{-1}$, varying the magnitude of R by a factor of 10. The boundary conditions and all other fluid parameters are kept fixed, while R is varied. When R is increased, the domain is cooled in the bulk and the average domain temperature decreases. Due to the decreased temperature, there is also lesser moisture in the domain, as q_s decreases with T and any moisture beyond the saturation specific humidity is rapidly removed by condensation.

Figure 2 shows instantaneous snapshots of the relative humidity (q/q_s) for two flows with $R = 1.5 \text{ K} \cdot \text{d}^{-1}$ (top panel) and $R = 3.6 \text{ K} \cdot \text{d}^{-1}$ (lower panel). The two snapshots are shown for the instant at which the largest vertical velocity w is realised throughout the run. Thus, the snapshots are not representative of the flow at other times. In particular, for the $R = 1.5 \text{ K} \cdot \text{d}^{-1}$ case, there are usually several smaller cloud plumes in the domain at most times (see Supplementary Movie 2). The snapshot shown here

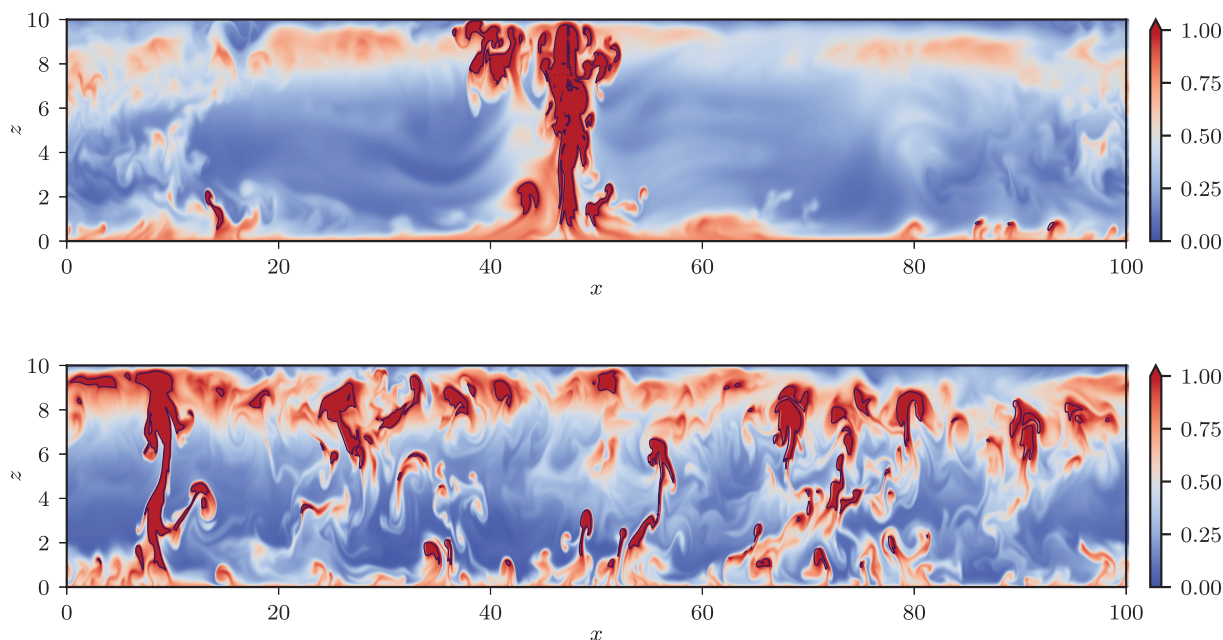


FIGURE 2 Instantaneous snapshots of the relative humidity (q/q_s) for two simulations with $R = 1.5 \text{ K} \cdot \text{d}^{-1}$ (top panel) and $R = 3.6 \text{ K} \cdot \text{d}^{-1}$ (bottom panel). The snapshots are taken at the time with the largest w value of the whole run. Dark solid lines represent clouds, that is, contours of $q/q_s = 0.98$.

is instructive in lending a hint about how extreme vertical velocities are generated. The largest values of w are usually realised within plumes that have a large vertical extent spanning almost the entire domain with a vertically contiguous region of supersaturation, such as the single plume in the top panel. For the lower panel, this extreme w is realised in the plume centred close to $x = 10$.

It is apparent from the snapshots that the flows with larger R have a much larger area undergoing convection. This can be seen by comparing the fraction of the domain occupied by the contours of 98% relative humidity. While there are no real clouds in the simulation, that is, we do not track condensed liquid water, it is still possible to study cloudy dynamics by considering “clouds” as grid points that are supersaturated, that is, where the condensation term in Equation (3) is non-zero. Due to the sharp discontinuity of this term, we henceforth define clouds as grid points with $q/q_s > 0.98$. While our analysis and results remain virtually unchanged if we include only supersaturated points, having a slightly lower relative humidity threshold gives greater cloud statistics.

We now recall the theoretical expectations for the response of a moist convecting atmosphere to increased radiative cooling. As mentioned in the Introduction, in clouds the total upward mass flux M_c is expected to increase linearly with radiative cooling. Indeed, in the concluding remarks of the work by Robe and Emanuel (1996),

the authors point out that, “The net upward mass flux carried by moist convection is strongly constrained by the requirement that the subsidence warming outside of the active condensation balance the radiative cooling.” For a Boussinesq fluid with constant density, the mass flux per cloud is simply proportional to the average upward velocity in clouds, which we denote w_c . If we denote with σ the area fraction of cloudy grid points at a given height, mass conservation yields

$$M_c = \sigma w_c = (1 - \sigma) w_{\text{sub}}, \quad (13)$$

where M_c is the cloudy upward mass flux and w_{sub} is the average downward vertical velocity outside clouds. The crux of Robe and Emanuel’s statement is that, since w_{sub} is unaffected by condensation, it must depend only on the radiative cooling. This can be seen by considering Equation (3) outside clouds. Far away from the vertical boundaries, we can neglect diffusion and, assuming that horizontal advection is small, the time and horizontal average of Equation (3) over the subsiding region gives

$$\langle w(\Gamma_d + \partial_z T) \rangle_{\text{sub}} \sim -R, \quad (14)$$

where $\langle \rangle_{\text{sub}}$ indicates the average over the clear-sky regions. For the average velocity w_{sub} outside clouds, we have

$$w_{\text{sub}}(\Gamma_d - \Gamma_m) \sim R, \quad (15)$$

where $\Gamma_m = -\partial_z T_{\text{sub}}$ is some typical (moist) value of the lapse rate of the domain outside clouds, which is meant to represent the moist adiabatic lapse rate in clouds. Indeed, moist convection in clouds is expected to bring the whole atmosphere towards this moist adiabatic lapse rate through gravity waves (Bretherton & Smolarkiewicz, 1989). Thus the lapse rate outside clouds is expected to match the moist adiabatic lapse rate in clouds. Combining Equations (13) and (15) yields

$$M_c = \sigma w_c \sim (1 - \sigma)R/(\Gamma_d - \Gamma_m). \quad (16)$$

If we assume that Γ_m remains fixed with R and $\sigma \ll 1$, this gives $M_c \sim R$, which is the oft-repeated statement that the cloudy mass flux increases in equilibrium with R .

3.2.1 | Scaling of convective mass flux

The above theoretical constraints on the total mass flux in clouds $M_c = \sigma w_c$ do not predict whether the upward mass flux increases due to an increase in the intensity of convection and faster updraughts (greater w_c) or through an increase in the amount of convection that occurs at a given time (greater σ), or a combination of the two effects. As mentioned in the Introduction, simulations in CRMs (Robe & Emanuel, 1996) have found that an increase in R leads to a large relative increase in σ , while w_c remains nearly fixed even for large variations in the magnitude of the imposed cooling.

Qualitatively, Figure 2 seems to indicate larger cloud fraction with stronger radiation in our simple model as

well. We quantify the variation in w_c , σ , and M_c for increasing R by measuring their individual relative changes, relative to their value in the simulation with the smallest R of $R_0 = 0.72 \text{ K} \cdot \text{d}^{-1}$. This is written as

$$\Delta\sigma/\sigma = \frac{\sigma(R) - \sigma(R_0)}{\sigma(R_0)}, \quad (17)$$

and similarly for w_c and M_c . The relative changes at height $z = 4.5 \text{ km}$ are shown in Figure 3a. This height corresponds to a strongly convective zone, where w_c is close to its maximum value in the vertical while σ is increasing with height. We consider this height as representative of the convective strength and it is analogous to the height selected by Robe and Emanuel (1996) for their analysis.

Figure 3a shows that the cloudy area fraction increases linearly with R , with a tenfold increase in R (or $\Delta R/R = 9$) leading to a tenfold increase in σ . w_c shows only a small change in magnitude, approximately doubling for the tenfold increase in R , while the convective mass flux M_c shows a superlinear increase. It is clear that the bulk of the contribution to the increased mass flux comes from the large increase in the cloudy area fraction, consistent with previous results from CRMs and observations. Additionally, we have checked for two cases ($R = 1.5 \text{ K} \cdot \text{d}^{-1}$ and $R = 3.6 \text{ K} \cdot \text{d}^{-1}$) that doubling the horizontal size of the domain leaves w_c and σ unchanged.

Figure 3b shows the variation of w_{sub} with R at the same height in the domain. The relative change in w_{sub} is > 20 , showing that the subsidence velocity increases far faster than the increase in magnitude of R . We compare the subsidence velocity with the theoretical estimate from Equation (15), with Γ_m taken to be the moist adiabatic

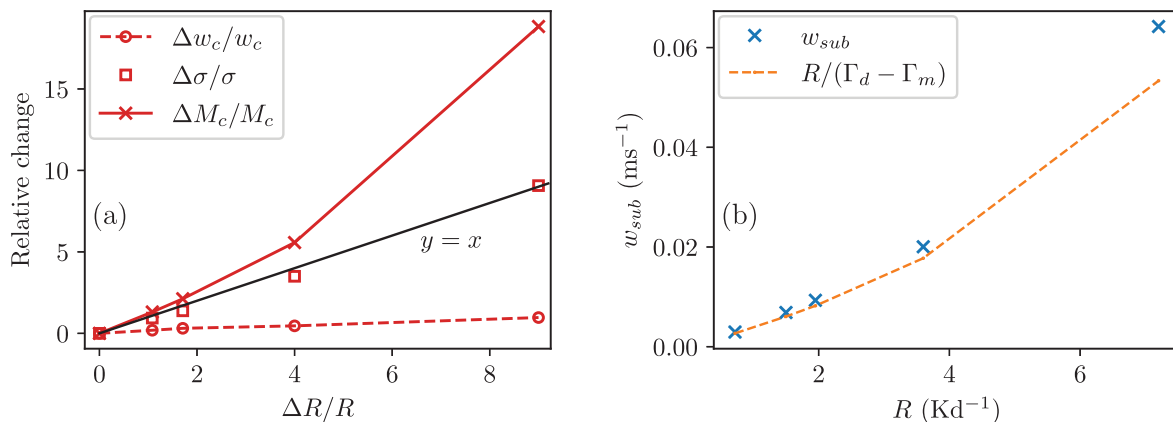


FIGURE 3 (a) The relative change in the cloud volume fraction σ , the time-averaged vertical velocity in clouds w_c , and the convective upward mass flux M_c measured at $z = 4.5 \text{ km}$. The $y = x$ line is shown for reference. (b) Average measured downward velocity outside clouds w_{sub} compared with a descent in equilibrium with radiation and lapse rate equal to Γ_m (see Equation 15) at $z = 4.5 \text{ km}$. Here, for Γ_m we use the theoretical moist adiabatic lapse rate for the domain average temperature measured in the simulation (see Equation 18).

lapse rate given by (see equation 3.4 of Val2019)

$$\Gamma_m = \frac{\Gamma_d}{1 + L_v \alpha q_s(\bar{T})}, \quad (18)$$

where \bar{T} is the measured horizontal average temperature at a given height. We emphasise here that the measured lapse-rate $-d\bar{T}/dz$ in the domain differs slightly from the theoretical moist-adiabatic lapse rate Γ_m —the measured value is about $1\text{K} \cdot \text{km}^{-1}$ steeper than Γ_m in all simulations—leading to an overestimate for w_{sub} .

This discrepancy comes from the fact that the average measured w_{sub} hides significant spatial variability in vertical velocity over the domain, while the theoretical estimates rely on the idealised assumption of a uniformly subsiding dry region outside clouds with perfectly coherent rising moist plumes within clouds. This small quantitative mismatch is interesting and deserves further investigation, but is beyond the scope of this study. For our purpose, it is sufficient to understand $(\Gamma_d - \Gamma_m)$ as just a multiplying lapse-rate scale for w_{sub} so the product scales as R . Note that w_{sub} itself thus scales approximately with R (Figure 3b), though not exactly. The value of Γ_m increases with R (moist-adiabatic lapse rate becomes less steep) due to the decrease in temperature at a given height—larger R leads to a colder domain, leading to a decrease in q_s and thus a moist lapse rate that is closer to the dry lapse rate.

It is therefore clear that, in a moist-convective system, the subsidence velocity outside clouds is set by a combination of R and the response of the temperature field to R . A tenfold increase in R also leads to a halving of $(\Gamma_d - \Gamma_m)$ (or a doubling of $(\Gamma_d - \Gamma_m)^{-1}$), which explains the large increase of w_{sub} . The subsidence velocity is thus directly sensitive to R and is also influenced by the changing lapse rate, which is an indirect effect of changing R . In summary, our results show that, consistent with theory and CRM simulations, the subsidence velocity scales approximately linearly with the radiative cooling amplitude, albeit with a slight change in the proportionality factor due to changes in the moist adiabatic lapse rate. As a consequence, the total cloud mass flux increases linearly with the radiative cooling amplitude, largely due to increased cloud fraction, while the average velocity in clouds remains largely insensitive to the radiative cooling rate. The small change over a large range of parameters is an indication that the convective velocity scale is likely set by small-scale, convective processes alone, a hypothesis that we investigate further next.

3.2.2 | Vertical velocity

The simple model of moist convection currently under investigation correctly captures the variation in the cloudy

mass flux with changing R , as results from previous work with CRMs have shown. The vertical velocity in the model as yet remains unconstrained and it still remains unclear what sets the updraught velocities. We investigate the velocity extremes and the distribution of vertical velocity in the domain for different R . In all the simulations, the median vertical velocity is slightly negative, with more than half of the domain being occupied by subsiding flows ($w < 0$). The up-down asymmetry is consistent with previous studies of dry stratified convection (Agasthya & Muller, 2024; Berengiero *et al.*, 2012), with the $-R$ term breaking the up-down symmetry (discussed further in Section 3.2.5). Further, the presence of moisture and condensation without evaporation in the model also leads to latent heating of rising parcels of fluids, without a corresponding evaporative cooling of subsiding parcels. This asymmetry exists in more complex models as well as in the true atmosphere, due to the fact that some of the condensates precipitate during ascent and are thus not present to evaporate during descent.

Convective available potential energy (CAPE) is an important measure used to characterise the instability of a column of moist air. CAPE is a vertical buoyancy integral calculated relative to a domain mean, where an idealised parcel is assumed to rise first dry-adiabatically ($\partial_z T = -\Gamma_d$), conserving its moisture content until it becomes saturated (i.e., reaches the dew point), following which the ascent is assumed to be moist-adiabatic ($\partial_z T = -\Gamma_m$, see Equation 18). CAPE is used to estimate the maximum kinetic energy such an idealised parcel can attain due to buoyancy lifting. In general, for a parcel ascent that follows a given rising parcel temperature profile $T_p(z)$, the buoyancy integral $B^i(T_p)$ up to a height z is given by

$$B^i(T_p) = \beta g \int_0^z (T_p(z) - \bar{T}(z)) dz. \quad (19)$$

The buoyancy integral leads to a prediction of vertical velocity given by $\sqrt{2B^i}$ for a parcel with temperature T_p lifted through a background temperature profile \bar{T} . While CAPE, calculated using the moist-adiabatic ascent, is commonly calculated for atmospheric soundings and to predict the intensity of impending thunderstorms, (Singh & O’Gorman, 2015) found a closer correlation between the buoyancy integral of temperature extremes and the maximum velocity in CRM simulations $B^i(T_{\text{extreme}})$.

Here, we compare the 99.999th percentile ($w_{99.999\text{th}}$) as well as the maximum vertical velocity (w_{max}) at each height with CAPE and the buoyancy integral velocity of the 99.99th percentile, 99.999th percentile, and maximum temperature attained at each height during the runs. The upper panels of Figure 4 show w_{max} and $w_{99.999\text{th}}$ for three values of R —the maximum w (red) remains remarkably

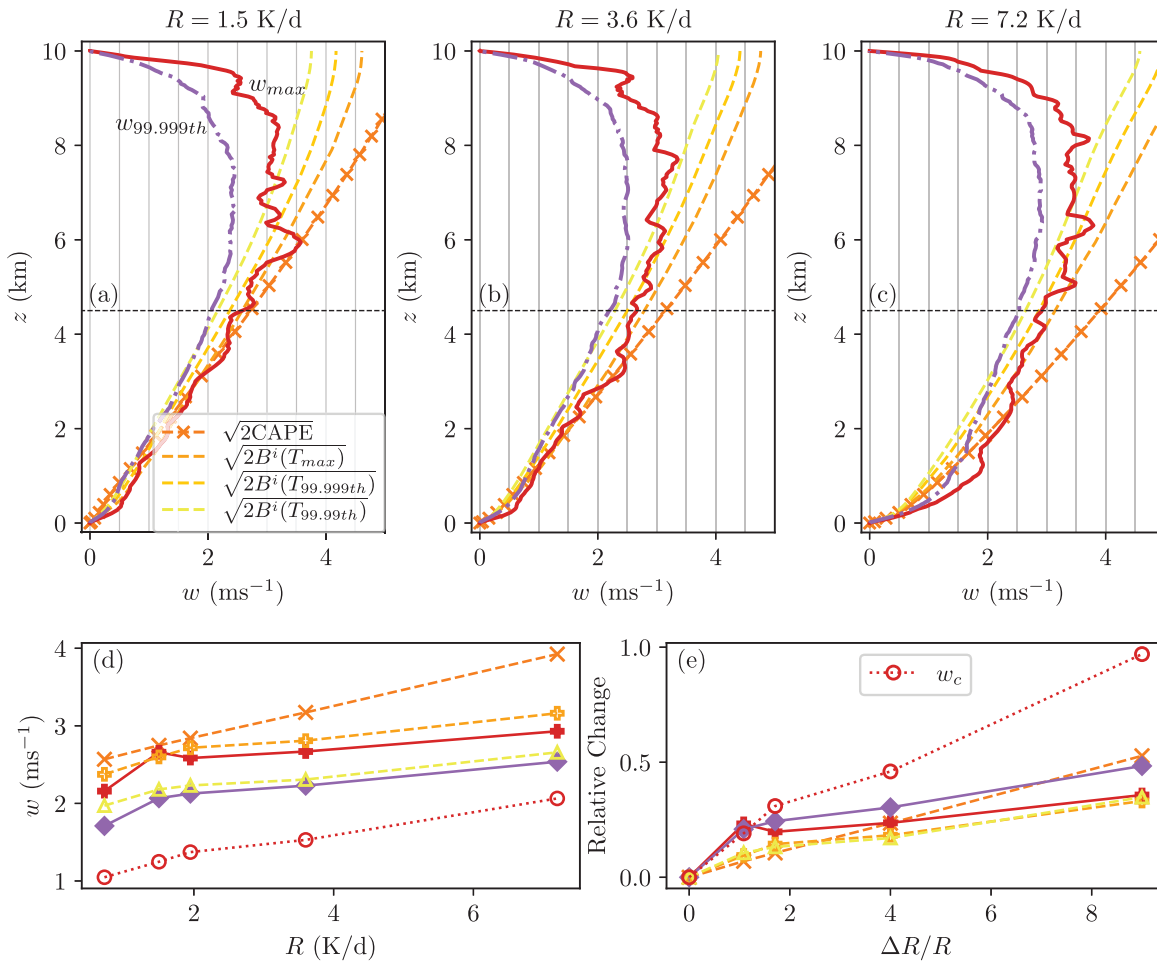


FIGURE 4 Maximum vertical velocity w_{max} (solid line) and the 99.999th percentile vertical velocity $w_{99.999th}$ (dotted line) at each height for (a) $R = 1.5 \text{ K} \cdot \text{d}^{-1}$, (b) $R = 3.6 \text{ K} \cdot \text{d}^{-1}$, and (c) $R = 7.2 \text{ K} \cdot \text{d}^{-1}$. This is compared with the velocity predicted by the buoyancy integral of the maximum, 99.999th, and 99.99th percentiles of temperature (dashed lines from left to right) and CAPE (crosses). Panels (d) and (e) show the values of the same quantities and their relative change respectively at $z = 4.5$ km, indicated by a horizontal dashed line in the upper panels, in addition to the average velocity in clouds w_c .

similar even for large variations in R , while the 99.999th percentile of w (purple) shows a small shift towards the right. These represent the most rapidly rising thermal plumes, with the fastest rising parcels without exception lying inside clouds. Even as the cloudy mass flux and the average downward velocity of the compensating subsiding flow outside clouds both increase by an order of 20, the maximum velocity in clouds as well as the average velocity in clouds remains stubbornly fixed independent of R . Zooming out momentarily, we found that the maximum vertical velocity at any height attained in the domain stays strictly between 3.2 and $3.9 \text{ m} \cdot \text{s}^{-1}$ even when T_{bot} is raised to 302.5 K or decreased to 297.5 K , when T_{top} is increased or decreased by up to 15 K , and even when κ is halved, for various imposed values of R (a detailed study of the dynamics of the model for varying parameters other

than R is not taken up in the current study). However, when βg was increased by a factor of 5, an approximate doubling of w_{max} was seen, indicating that w_{max} is most closely related to the buoyancy integrals and the mechanism that sets the temperature anomaly of the cloudy rising plumes.

Figure 4 also shows the vertical velocity predicted by CAPE, as well as the buoyancy integrals of the highest percentiles of T . CAPE (orange crosses) seems like an excellent prediction for w_{max} for $R = 1.5 \text{ K} \cdot \text{d}^{-1}$, as seen in Figure 4a. This result, however, is not robust when R is varied, as shown in Figure 4b,c, where CAPE is a large overestimation of the vertical velocity. The buoyancy integrals of the temperature extremes (going from yellow to orange) predict the highest velocity percentiles extremely well, up to $z \sim 6$ km. The departure

of the temperature extremes from the domain average temperatures (not shown) is also independent of R . Figure 4d shows the values of w_{\max} , $w_{99.999\text{th}}$ and the buoyancy integral velocities at $z = 4.5$ km as a function of R , while Figure 4e shows the relative change of these quantities as a function of the relative change in R . CAPE at a fixed height increases linearly with increasing R —the increase is due to the fact that the domain becomes colder on average, while the temperature of a moist adiabatic ascent remains fixed for the same boundary conditions. The magnitudes of buoyancy integral velocities follow the extreme vertical velocities closely, with the 99.99th percentile of temperature (yellow) being an excellent predictor of the 99.999th percentile of w (purple). We also show the average velocity in clouds w_c for readers to make a comparison with Figure 3a while noting the change in the y -axis range.

The extreme velocities show a small increase ($\sim 50\%$) over the parameter range, which is broadly similar to the growth in buoyancy integrals and in CAPE. However, the majority of this increase happens in going from $R = 0.7 \text{ K} \cdot \text{d}^{-1}$ to $R = 1.5 \text{ K} \cdot \text{d}^{-1}$, following which the extreme velocities remain nearly constant while CAPE continues to grow linearly. It is important to note here that, even if w_{\max} grew similar to the CAPE velocity, the relative increase is still very small compared with the increase in σ and M_c discussed in the previous section. Importantly, regardless of the buoyancy estimate used to predict w changes, these integrals are constraints on vertical velocity, preventing its strong increase with R , and are responsible for the fact that the increased mass flux is achieved almost entirely through increased cloud fraction.

3.2.3 | Velocity in individual clouds

In the previous section, we considered buoyancy integrals of the temperature extrema from the entire simulation run and found that these integrals scale very closely with the extrema of vertical velocities from the simulation. While this gives us cause for cautious optimism, it must be noted that the profile of the maximum or 99.999th percentile of temperature does not correspond exactly to any single instant in the simulation. Here, we exploit the simplicity of our idealised set-up to investigate individual clouds to find the correlation between the maximum velocity within a cloud plume and the buoyancy integral of this cloud. Noting that the horizontally averaged temperature profile \bar{T} shows little variation in time, we measure the buoyancy integral for individual clouds from the maximum temperature attained at each height in the cloud. At leading order, the balance between the advection term and the buoyancy term in the vertical component of the momentum equation

(Equation 2) leads to

$$\begin{aligned} w \partial_z w &\approx \beta g (T(z) - \bar{T}) \implies \frac{1}{2} (w(z)^2 - w(z_0)^2) \\ &\approx \beta g \times \int_{z_0}^z (T(z) - \bar{T}(z)) dz, \end{aligned} \quad (20)$$

where z_0 is the height of the cloud base. Then, in a given cloud, the parcel with the fastest vertical speed of ascent w_B should correspond to an upward-moving parcel, which begins at z_0 with vertical velocity w_0 and accelerates at a rate predicted by the buoyancy integral calculated with respect to the maximum temperature in the cloud at the given height. This leads to

$$\max_x (w(z)) \approx w_B(z) \equiv \sqrt{w_0^2 + 2B(z)}$$

with

$$B(z) = \beta g \times \int_{z_0}^z \max_x (T(z) - \bar{T}(z)) dz, \quad (21)$$

where $\max_x f$ is the maximum of the function f at a fixed height within the given cloud. Thus, w_B is a prediction for the maximum velocity inside a cloud, given a profile of the maximum temperature inside the same cloud.

Figure 5a shows the snapshot of the temperature anomaly of a single “well-behaved” cloud from the simulation with $R = 1.5 \text{ K} \cdot \text{d}^{-1}$, with the location of the vertical velocity maximum corresponding well with the regions shaded with the deepest red colour (warmest). A cloud is defined as a contiguous region with $q/q_s > 0.98$, as in the rest of the study. Additionally, we also impose the condition that a cloud must contain at least one supersaturated ($q/q_s > 1$) grid point. This ensures that there are no single grid-point clouds and the buoyancy statistics are considered only where condensation is playing a role in the dynamics. Clouds were identified using the “skimage.measure.regionprops” function of the scikit-image Python package (van der Walt *et al.*, 2014). Figure 5b shows the maximum vertical velocity at each height within the cloud, compared with the prediction w_B from Equation (21). We see that the predicted w_B matches the measured w_{\max} excellently up to about the height at which the cloud w_{\max} profile reaches its maximum value in z . The horizontal location of the w maximum in the cloud (indicated by the black, dashed line in Figure 5a) also indicates that this corresponds to a single, vertically rising warm parcel. Above this height, which we denote as z_{\max} , w_{\max} falls off, as the plume does not remain as coherent and the temperature anomaly of the cloud decreases due to a combination of adiabatic cooling of the fast-rising parcel, the decrease in moisture content due to condensation,

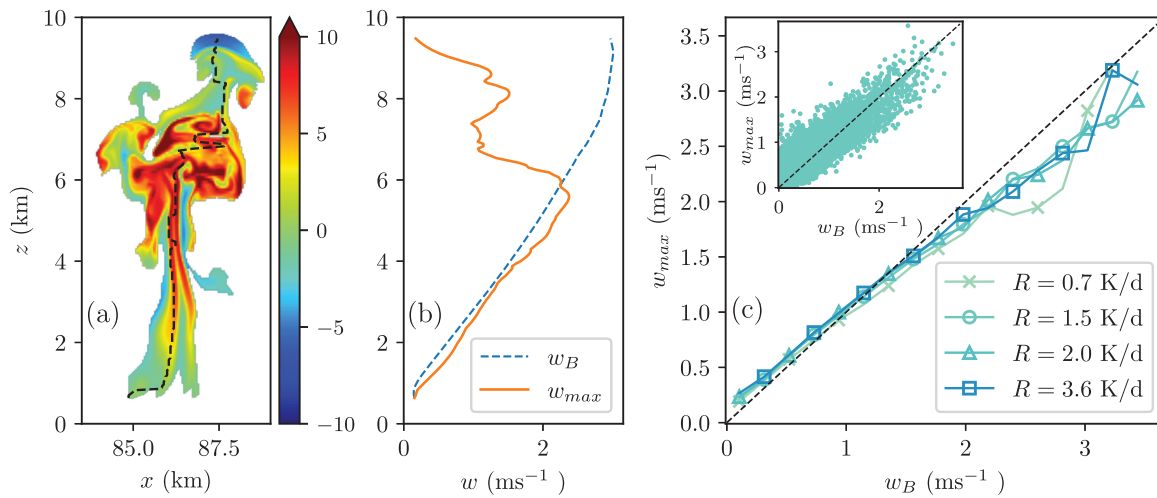


FIGURE 5 (a) Temperature anomaly with respect to domain and time-average horizontal mean in a chosen cloud plume. The boundary of the cloud is the contour of 98% relative humidity and the black dashed line shows the location of the maximum w within the cloud at a given height. (b) The maximum velocity w_{\max} at each height for the cloud plume in panel (a) compared with the predicted vertical velocity w_B from the buoyancy integral. (c) The inset shows the scatter plot of w_B and w_{\max} within the cloud for all clouds in the simulation with $R = 1.5 \text{ K} \cdot \text{d}^{-1}$ with $w_0, B > 0$. The main figure in panel (c) shows the same horizontally binned average of the same scatter plot for other values of R . The dashed line represents the $y = x$ line.

and turbulent entrainment of non-cloudy air at the edge of clouds.

While w_B (blue, dashed curve in Figure 5b) matches w_{\max} (orange, solid curve) very closely, it is still a small overestimate. This is expected, given that a perfect balance between vertical advection and the buoyant forcing is an idealisation, with diffusion, lateral mixing, and non-hydrostatic pressure-gradient forces still playing a part.

Figure 5a,b considers the behaviour of a single, well-chosen cloud plume, which shows close to ideal behaviour. To understand the overall behaviour of clouds better, we consider all clouds in the simulation (sampled every 0.5 hours) and calculate the buoyancy integral B up to the height z_{\max} at which the profile of w_{\max} within the cloud attains its maximum value. Since we are interested in upward-moving plumes accelerated by buoyancy, we choose those clouds that have w_0 and $B > 0$. The inset to Figure 5c shows a scatter plot of w_B on the x -axis and the maximum velocity w_{\max} for all clouds for the simulation with $R = 1.5 \text{ K} \cdot \text{d}^{-1}$. All points lie near a line of slope unity (dark-dotted line). In the main panel, we present the same data for varying R —the data are binned into intervals of uniform w_B and the average w_{\max} for a given bin is plotted. Again, for all R , the curves match almost exactly with the line of slope unity, with w_B being a small underestimate of w_{\max} for clouds with smaller w_B and an overestimate for clouds with larger w_B . While the high frequency of sampling can lead to the same cloud plume being sampled multiple times over the course of its development, we have

checked that the result is robust even when the sampling frequency is decreased to once every 20 hours, where each consecutive snapshot is well decorrelated.

We found that larger values of w_B (and hence w_{\max}) correspond to taller clouds, while the smaller values correspond to clouds with a small vertical extent. The reason that w_B remains an overestimate for w_{\max} in taller clouds has been discussed above. For smaller clouds, we hypothesise that the underestimate comes from smaller clouds that develop close to the lower boundary and are accelerated upward by low-level horizontal convergence. We must also note that the maximum vertical velocities here are achieved by the upward acceleration of air parcels during the evolution of the cloud plume, while we estimate the cloud buoyancy using a frozen-in-time snapshot of the temperature anomaly of the plume. The implicit assumption here is that the vertical structure of the temperature anomaly in the plume does not vary greatly in time. While the close match between w_B and w_{\max} suggests that the assumption is reasonable, caution must be exercised in drawing conclusions from this calculation. We have further checked that the same correlation holds for w_{\max} for the same cloud with the measured instantaneous cloud buoyancy at prior times in the simulation, up to 10 simulation units prior.

Overall, the above results remain broadly consistent with our hypothesis that, in individual cloud plumes, it is small-scale temperature perturbations and anomalies exclusively that drive the dynamics of the plume, with minimum impact from large scales. This is true not only

of velocity extremes over the whole run, but also of the velocity extreme in each cloud plume.

3.2.4 | Predictions from entraining plume models

In previous sections, we saw that the changes in vertical velocities in updraughts were small and showed quantitative agreement with buoyancy integrals. However, estimating these buoyancy integrals requires the knowledge of maximum temperatures or high temperature percentiles in addition to the average temperature profile. Further, we have seen above that, for a tenfold increase in R , the average vertical velocity in clouds and the vertical velocity of the fastest rising parcels show a slow increase even as the area of the domain showing moist convection increases with R . The main impact of the variation in R is the change in the temperature profile—the domain becomes colder for larger R . Since we calculate the temperature profile of a moist-adiabatic ascent from the surface where the surface temperature and moisture boundary conditions do not change, the theoretical moist-adiabatic profile stays fixed for varying R . This cooling of the domain thus leads to an increase in CAPE.

Unlike CRM simulations, where surface fluxes are parametrised using bulk formulas, our simulations develop a dissipative boundary layer where T and q decrease steeply. Calculation of CAPE assumes ascent along a dry adiabat from the surface up to the lifting condensation level (LCL), followed by ascent along a moist adiabat. In our case, instead of following a dry adiabat to the LCL, surface parcels are strongly affected by diffusion, as the diffusive boundary layer covers a significant fraction of the sub-cloud layer ($\sim 50\%$) and the lapse rate in this layer is significantly steeper than the dry adiabatic one. The gradients in the diffusive layer also become steeper with increasing R , in accordance with Equation (11). Attempts to construct modified moist-adiabatic ascents using the domain-average temperature profile from above the dissipative layer, for example, starting from the height of lowest cloud formation from the simulation or from the height at which the domain-mean temperature first reaches the dew point corresponding to q_{bot} , also yield poor predictions of w_{max} for varying R .

Here, we attempt to improve our quantitative estimates of maximum velocity based on a theoretical estimate of CAPE that accounts for the environmental temperature profile as well as entrainment, which is the mixing of non-cloudy, drier, and colder air from the environment into cloud plumes. Entrainment is an important process in the ascent of cloud plumes, one that we expect to play a significant role in our case, where the temperature of

the environmental air varies significantly with variation in R . We thus investigate the changes in vertical velocities further in light of recent theoretical developments on what sets the strength of updraughts (Singh & O’Gorman, 2013, 2015).

Singh and O’Gorman (2013) introduced a model to quantify the effect of entrainment on undilute ascent. The model begins by assuming that the atmosphere is composed mainly of dilute cloud plumes, which entrain environmental air at a typical rate of $\epsilon \text{ km}^{-1}$. The rapid equilibration of the horizontal temperature field by gravity waves means that cloud plumes on average have zero buoyancy relative to the environment. In our set-up, where there are no virtual effects, this simply translates to the clouds and the environment being at the same temperature. (This is true in our simulations, where the average temperature anomaly in clouds is a very small positive value.) Thus, the temperature profile of the entire domain is identical to that of a cloud plume with this typical entrainment rate of ϵ .

The maximum vertical velocity then arises from the ascent of a fully undilute (0 entrainment) plume in this environment. The temperature anomaly ΔT_u of this undilute plume with respect to the environment follows the relation

$$\frac{\partial}{\partial z}(\Delta T_u) = \frac{\epsilon L_v}{1 + \alpha L_v q_s(\bar{T})} (1 - R_e) q_s(\bar{T}), \quad (22)$$

where R_e is the horizontal domain average relative humidity and \bar{T} is the average temperature at a given height z . ΔT_u is proportional to the entrainment rate, because an undilute plume in an atmosphere with more entraining cloud plumes is relatively more buoyant than an undilute plume in an atmosphere with less entraining cloud plumes. This approach has the added advantage that it requires only an estimation of the domain-averaged temperature profile and not any other measurements from the simulations, such as the high-percentile temperature values.

We use a fixed $R_e = 0.4$, which is a typical value of relative humidity in the bulk of the domain. We have checked that replacing R_e with the measured, vertically varying value from the simulations does not affect the results significantly. Assuming entrainment to be inversely proportional to height (Holloway & Neelin, 2009; Singh & O’Gorman, 2013), we estimate ΔT_u by starting the integration from the theoretical LCL for the given boundary conditions ($z = 0.404 \text{ km}$). The actual height of the first instance of condensation remains below 500m in the simulations for all R . The estimate of ΔT_u leads to a prediction for w_{max} via the buoyancy integral as given by Equation (19).

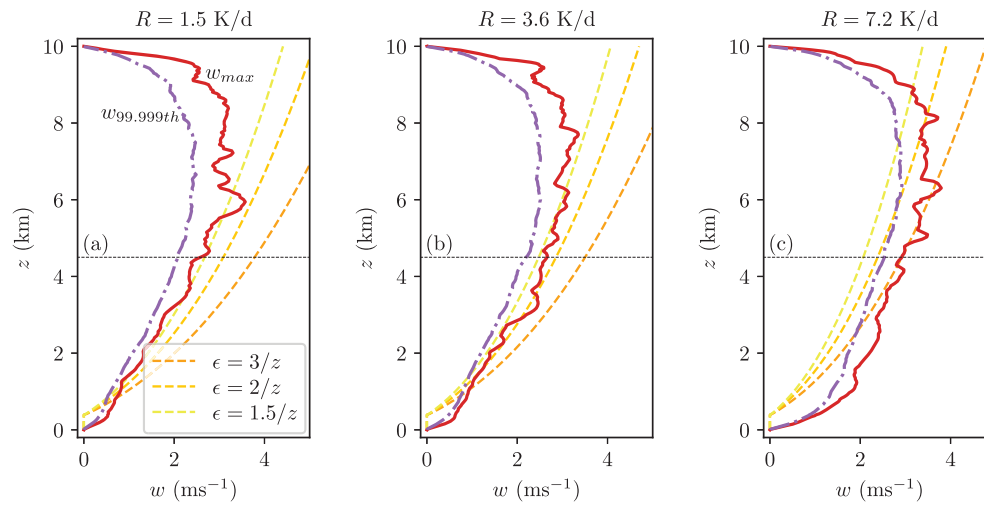


FIGURE 6 Maximum (solid curve) and 99.999th percentile (dotted line) vertical velocity at each height for the entire simulation run compared with the estimated vertical velocity from the buoyancy integral for a parcel with temperature anomaly given by Equation (22) with three different entrainment rates ϵ for (a) $R = 1.5 \text{ K} \cdot \text{d}^{-1}$, (b) $R = 3.6 \text{ K} \cdot \text{d}^{-1}$, and (c) $R = 7.2 \text{ K} \cdot \text{d}^{-1}$.

Figure 6 shows the predicted velocity using the temperature of the undilute plume ascent for three different values of ϵ for three values of R . The predicted velocity is 0 until the height of the LCL, following which it increases to match w_{\max} very closely between $z \sim 3$ and 6.5 km, with the closest matching ϵ increasing for increasing R . Higher entrainment for higher R flows can be expected from the increased area undergoing convection, which leads to greater turbulent kinetic energy and mixing and a lower typical distance between plumes, which leads to the inter-plume region being less quiescent. If we assume as given that an entraining plume sets the environmental temperature, the above results can be understood as an estimate for the degree of entrainment in clouds in the simulations, with enhanced entrainment (ϵ going from approximately $1.5/z \text{ km}^{-1}$ to $3/z \text{ km}^{-1}$) arising for larger R . Importantly, we see that to have large increases in w_{\max} with increasing R would need relatively large changes in the entrainment rate as suggested by the above plume model.

3.2.5 | Comparison with dry convection

Finally, to understand the effect of moisture on convection, we compare the moist simulations with their corresponding dry simulations, which are run with all parameters identical except L_v , which is set to zero, so that moisture is now a passive tracer without any impact on the dynamics, given that virtual effects are ignored in the model. Uniformly cooled dry convection, known as the Prandtl system, is a well-studied system in fluid dynamics literature and finds several applications in the study of the atmospheric boundary layer (see chapter 3 of (Emanuel, 1994)). The differences in stability and heat transfer between the dry and moist simulations are also of broader interest to

researchers interested in the study of models of thermal convection, with possible applications to other natural settings. These differences could also hold insights into the dynamics of atmospheric moist convection.

Figure 7a shows the histogram of the vertical velocity for values of R for the dry case (dashed lines) as well as the moist case (solid lines). Both histograms peak to the left of $w = 0$, with the median velocity being negative (downward). The distributions of the dry systems are flatter near $w = 0$, with the tails of the distribution being nearly symmetric. We note in passing that the dry case without radiative cooling has an up-down symmetry (the system remains invariant under the transformation $T \leftarrow -T, z \leftarrow -z$), and interior cooling breaks this symmetry (Agasthya & Muller, 2024; Berlingiero *et al.*, 2012). The moist distributions, on the other hand, are more sharply peaked, with broad tails. The asymmetry is also more pronounced, with the positive tail of the moist distribution being broader than the negative tail. Physically, this additional up-down asymmetry in the moist case comes from precipitation. Upward convection is associated with condensation and concomitant release of latent heat, thus occurring on a moist adiabat. However, since all condensates are assumed to precipitate instantaneously in our simple model, the downward convection does not contain condensates or the corresponding latent cooling from evaporation, and instead occurs on a dry adiabat. Note that the up-down asymmetry in moist convection is also consistent with energetic arguments, even in the absence of interior radiative cooling (Bjerknes, 1938).¹

Variation in R also impacts the histograms. Increasing R increases the overall convection in the domain, as measured by the convective heat flux \overline{wT} , leading to larger kinetic energy and greater velocities on average. This is seen as a flattening of the distribution of w and a shift of

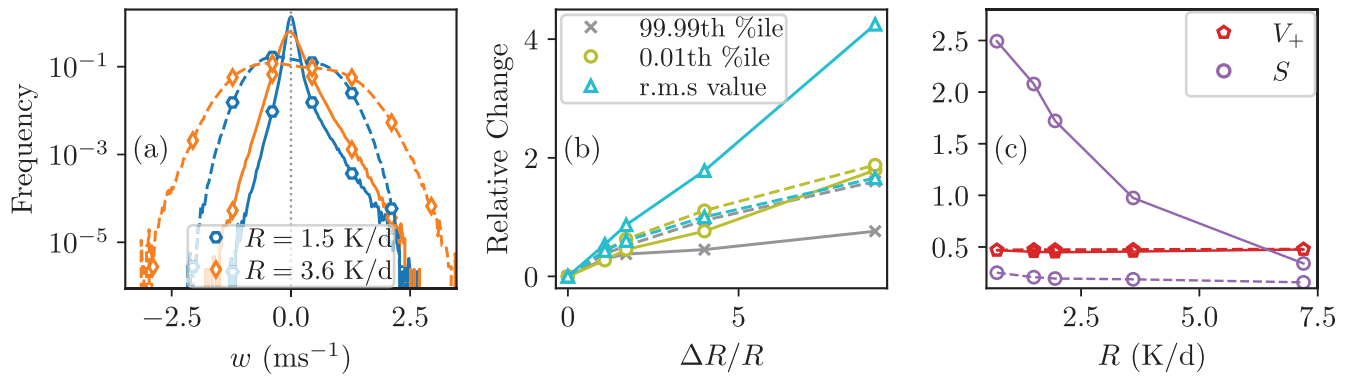


FIGURE 7 Figure showing comparison of the statistics of vertical velocity w measured at height $z = 4.5\text{km}$ for moist simulations (solid lines) and dry simulations (dashed lines). (a) Normalised log histogram of simulations for two different values of R (see legend). The dotted vertical line shows $w = 0$. (b) Relative change in the value of the 99.99th percentile, 0.01th percentile, and the root-mean-square value of w plotted against relative change in R . (c) The fraction V_+ of grid points with $w > 0$ and the skewness plotted against R .

the median w slightly to the left. It is worth noting that, in the dry case, both the positive and the negative ends of the distribution shift outward for an increase in the magnitude of R . However, in the moist case only the negative end of the distribution shifts significantly, while the positive extrema remain nearly fixed—this phenomenon in the moist case has been discussed in detail in the previous sections. We can quantify the shift in the distribution by looking at their relative changes. Figure 7b shows the relative change in the 0.01th percentile, 99.99th percentile and the root-mean-square (r.m.s.) value of w at a fixed height for dry and moist simulations.

Indeed we see that, in the dry cases (dashed lines), increasing R leads to a proportional increase in the fastest updrafts (99.99th percentile) and the fastest downdrafts (0.01th percentile), along with an increase in the typical magnitude of w as measured by its r.m.s. value. The subsiding branch of the moist distribution behaves similarly to the dry distribution, while the r.m.s. value shows a large increase compared with the dry simulations.

Finally, in Figure 7c we study the fraction V_+ of the domain that has w positive (red curves). We emphasise here that the area fraction V_+ is different from the cloudy area fraction σ discussed in earlier sections—the latter is a feature of moist convection alone and is closely associated with moist convective plumes. V_+ on the other hand includes any point in the domain that is instantaneously moving upward, even far away from clouds or convective plumes, which could be caused either by turbulent fluctuations or gravity waves. Such upward motion does not necessarily lead to condensation. For both moist and dry simulations, V_+ lies just below 0.5. This asymmetry has been studied previously (see (Agasthya & Muller, 2024)), wherein highly convective, turbulent flows have nearly

half of the domain moving upward even in the presence of a strong up–down asymmetry. A better measure of the asymmetry is the skewness measure S , also shown in Figure 7c (purple curves). The skewness of the dry and moist simulations decreases with increasing magnitude of R . However, the skewness in the moist case is far higher, indicating a greater degree of asymmetry in the dynamics.

In the dry case, the large-scale balances given by Equations (11) and (12) are still valid, with the moisture terms dropping out of the equations. To compare the dry and moist simulations further, we revisit the heat-transfer equation (Equation 12), which when averaged over the entire domain and divided throughout by the product RL_z gives

$$\frac{\langle wT \rangle}{RL_z} + L_v \frac{\langle wq \rangle}{RL_z} + \frac{\kappa \Delta T}{RL_z^2} + L_v \frac{\kappa_q \Delta q}{RL_z^2} = \frac{1}{2} + C_1. \quad (23)$$

Here $\langle \cdot \rangle$ represents the domain average of a quantity, ΔT and Δq are the temperature difference $T_{\text{bot}} - T_{\text{top}}$ and the moisture difference $q_{\text{bot}} - q_{\text{top}}$, respectively, while C_1 is a constant proportional to C_0 given by $C_0/(RL_z^2)$. We remind the reader that C_0 represents the total heat flux (sensible + latent) at the upper boundary and thus C_1 is the (negative of the) average non-dimensionalised heat flux out of the domain at the top boundary for each simulation.

The four terms on the LHS are non-dimensionalised heat fluxes. The first two terms represent convective heat fluxes and the next two terms represent conductive heat fluxes, normalised by the net radiative cooling. We henceforth refer to these quantities as Term1, Term2, Term3, and Term4 respectively. The scaling of non-dimensionalised heat fluxes (usually referred to as the Nusselt number in

TABLE 2 The first four columns show the non-dimensional values of convective sensible heat flux, convective latent heat flux, conductive sensible heat flux, and conductive latent heat flux corresponding to the four terms of Equation (23) for the different values of R in the dry and moist simulations. The last column shows turbulent kinetic energy given by $\langle |\mathbf{u}|^2/2 \rangle$ in $\text{m}^2 \cdot \text{s}^{-2}$.

R ($\text{K} \cdot \text{d}^{-1}$)	Term1		Term2		Term3		Term4		TKE ($\text{m}^2 \cdot \text{s}^{-2}$)	
	$\langle wT \rangle / (RL_z)$		$L_v \langle wq \rangle / (RL_z)$		$\kappa \Delta T / (RL_z^2)$		$\kappa_q L_v \Delta q / (RL_z^2)$		Dry	Moist
	Dry	Moist	Dry	Moist	Dry	Moist	Dry	Moist	Dry	Moist
0.72	0.1018	0.0235	0	0.2188	0.0933	0.0933	0	0.0864	0.0916	0.013
1.5	0.1074	0.0282	0	0.2807	0.0448	0.0448	0	0.0415	0.194	0.0283
1.95	0.1072	0.0309	0	0.2898	0.0345	0.0345	0	0.0319	0.2476	0.0376
3.6	0.1013	0.0320	0	0.300	0.0187	0.0187	0	0.0173	0.402	0.0685
7.2	0.0933	0.0395	0	0.2782	0.0093	0.0093	0	0.0086	0.7204	0.2054

the literature) has been studied widely for diverse models of thermal convection (Bouillaut *et al.*, 2019; Shraiman & Siggia, 1990), including Rainy–Bénard convection (Vallis *et al.*, 2019). While we do not explore wide ranges in the parameter phase-space, we believe that the variation of these fluxes for the changes in R that we impose can be the starting point for researchers interested in studying the behaviour of a moist internally cooled convective system.

In Table 2, we compare these terms for the dry and moist simulations. For the dry case, Term2 and Term4 are identically 0, since there is no moisture in the domain. Since ΔT is kept fixed, Term3 remains the same for both dry and moist simulations for each value of R and decreases as $1/R$.

For the dry simulations, Term1 remains nearly fixed, showing an overall small decrease, with a small increase from $R = 0.72 \text{K} \cdot \text{d}^{-1}$ to $R = 1.5 \text{K} \cdot \text{d}^{-1}$ followed by a monotonic decrease. This indicates that the convective heat flux scales sublinearly with R . The sum of Term1 and Term3 always remains lower than 0.2 and both terms decrease with R , indicating that the fluxes at the boundaries are the dominant contribution to balancing the radiative cooling, since from Equation (23) this requires $|C_1| > 0.3$. This contribution also become increasingly larger for larger R . For the moist simulations, on the other hand, Term1 increases significantly with increasing R , while Term2 increases until $R = 3.6 \text{K} \cdot \text{d}^{-1}$ and then decreases. We would expect that the term would continue to decrease for even larger R as the domain becomes colder, hence drier, and its behaviour starts to approach the dry system. The regime for the first four values of R , where both Term1 and Term3 increase in tandem, is interesting and deserves further investigation. We hypothesise that, initially, increasing R acts by strongly destabilising the column of fluid, leading to more convective plumes, which lead to more dry convection, and condensation due to the

rising plumes leads to increased latent heat flux. Why this trend is opposite in dry convection and at what values of R the drying effect become dominant is an open question that is beyond the scope of the current study.

Finally we note that the sum of the four terms is larger in the moist simulations compared with dry convection, decreasing from 0.42 to 0.33 from the smallest to the largest value of R . This indicates that the boundary heating contribution is less important, which is expected given that condensation acts as an extra source of heating within the domain. The latent heat convective flux (Term2) is indeed the dominant contribution to the heat balance.

While in both cases the net heat transfer is identical and is set by the large-scale balances with R , in the moist case the transport of moisture also contributes to heat transfer by latent heating. A moist updraught simultaneously transports sensible and latent heat upward. For this reason, the dry systems have a larger kinetic energy and need to have more convection, as indicated by Term1 being larger in magnitude in the dry simulations. The final column in Table 2 shows the domain-averaged dimensional turbulent kinetic energy (TKE) for each value of R . As expected, the moist simulations have a lower TKE compared with the dry simulations. We also see that the moist simulations show a superlinear increase in TKE with R , where, for a tenfold increase in R , there is a 15-fold increase in TKE. This is in contrast to the dry simulations, where the increase is sublinear. Figure 8 shows instantaneous temperature and vertical velocity snapshots of moist convection (left panels) and dry convection (right panels). The moist case shows one strong rising hot, moist plume and a broad region of subsidence outside this plume, whereas the dry convection has an equal number of rising and subsiding coherent plumes, respectively. This is consistent with the large difference in the skewness measure and the larger magnitude of $\langle wT \rangle$ and TKE in the dry simulations.

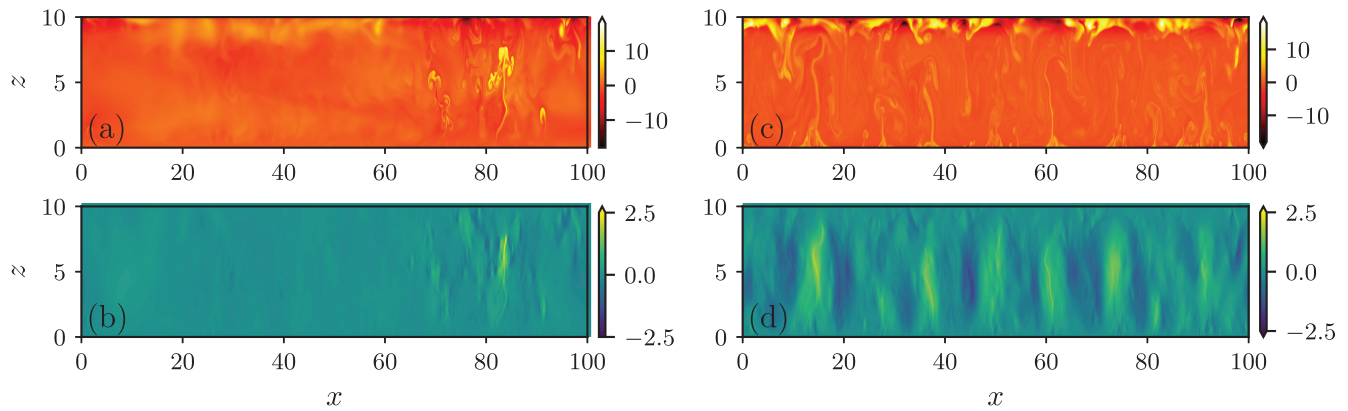


FIGURE 8 Instantaneous snapshots of the heightwise temperature anomaly in K (top panels) and vertical velocity in $\text{m} \cdot \text{s}^{-1}$ (lower panels) for dry simulations (left panels) and moist simulations (right panels) for the case of $R = 1.5\text{K} \cdot \text{d}^{-1}$.

4 | CONCLUSION AND DISCUSSION

We have presented here a study of Rainy–Bénard convection, introduced by Vallis *et al.* (2019), in line with several similar models that have been studied earlier. We run simulations for realistic fixed boundary temperature and moisture boundary conditions on a two-dimensional (2D) domain with aspect ratio 10 and vary the radiative cooling R . We analyse and present the results for five different values of R . The boundary conditions and parameters are chosen such that, in the absence of radiative cooling ($R = 0$), the system is conditionally unstable to moisture, that is, the dry system is stable and the moist system is unstable without steady convection (the domain alternates between long phases of quiescence and short bursts of convection). For the smallest value of (non-zero) R studied here, the dry system without moisture and the moist system show steady convection (convection occurring in the domain at all times). Thus, the parameters chosen are such that the underlying, stable dry Rayleigh–Bénard system is destabilised simultaneously by both the introduction of moisture and bulk radiative cooling.

We characterise the changing behaviour of the system for varying R , in particular the change in the time-averaged profiles of the prognostic variables temperature and specific humidity. In line with previous findings from CRM simulations as well as observations, we find in our simplified model that the intensity of convection, measured by the average upward velocity in clouds, increases much more slowly than R , while the cloudy area fraction, measured as the fraction of points having relative humidity $q/q_s > 0.98$, increases at a similar rate to R . The corresponding increase in cloudy mass flux (vertical velocity times cloudy area) can be related through mass conservation to increased subsidence velocity. The average

subsidence velocity outside clouds increases with increasing R , with a magnitude closely following the theoretical prediction from the heat equation in the absence of condensation. This leads to the cloudy mass flux increasing approximately linearly with R (albeit slightly faster due to decreased $(\Gamma_d - \Gamma_m)$, see Section 3.2.1), with the increase being dominated by the increase in cloudy areas of the domain.

We also investigate the maximum vertical velocity in the simulations for different R , finding that the upward velocity extremes remain nearly constant, with an increase even slower than the average velocity in clouds. This was compared with the convective available potential energy (CAPE) and it was found that the prediction from CAPE was an overestimation, with CAPE increasing uniformly with increasing R while w_{max} remained fixed. The buoyancy integrals of the extreme temperatures were instead found to predict the extreme vertical velocities closely, consistent with earlier findings in CRMs (Muller *et al.*, 2011; Singh & O’Gorman, 2013). Extreme vertical velocities within individual cloud plumes were also found to be closely related to the buoyancy integral of the extreme temperature anomaly within the same cloud, showing that the mechanism holds even for a single plume and not only as a large-scale statistic.

The physical factors that set the maximum temperature remain an open question. In the study we provide one possible explanation based on the ascent of an undilute plume in an environment set by an entraining plume model, following and adapting ideas introduced by Singh and O’Gorman (2013). Importantly, regardless of the buoyancy estimate used for w in updraughts, all the estimates change only weakly with R , providing constraints from convective physics that limit the increase in w and explain why the convective mass flux increase is reached almost entirely through increased cloud area.

Finally, we compare the behaviour of the moist model with the corresponding dry simulations, which sheds light on the degree of up–down asymmetry inherent in the system. Both the $-R$ term in the equations and the asymmetry between condensation and evaporation lead to an up–down asymmetry. We find here that, while the dry simulations with radiative cooling are well into the turbulent convective regime and have only a small degree of up–down asymmetry in the vertical velocity, as measured by the frequency of rising parcels of fluid or the skewness of the vertical velocity, the moist simulations show a larger degree of up–down asymmetry for all R , with the behaviour of the moist system converging towards dry convection for increasing R . We also note the varying heat-transfer characteristics and the kinetic energy differences across the dry and moist simulations.

The main drawback of using idealised models with direct numerical simulation as an atmospheric model is the requirement for very fine resolution grids to have realistic values of molecular diffusivity and conductivity. In the absence of such high resolution or parametrisation of subgrid fluxes, we are forced to set κ and ν to unrealistically large values, with the most immediate effect being the presence of a diffusive boundary layer ($\sim 200\text{m}$ high) that is far larger than the atmospheric skin layer (usually a few metres thick). This impacts the relative humidity and temperature profile in the convective bulk, leading to measured values in the simulations that can differ from realistic atmospheric values even when we impose realistic temperature and moisture boundary conditions and values of R . The large values of diffusion in the model also decrease the effective Reynolds number of the flow and thus alter the turbulence characteristics of the flow. Comparison with more complex CRMs and finer resolution direct numerical simulations is desirable to investigate the role of boundary layers, surface fluxes, and small-scale turbulent fluctuations further. We still find that our 2D idealised model shows realistic behaviour in its response to changing R and various convective processes. Further, simple models can be used as a starting point in the analysis of basic fluid instabilities.

Future avenues of investigation, which retain the simplicity and ease of implementation of the current approach, include the response of the system to varying boundary conditions and changing fluid parameters, such as β , ν , κ to more realistic values by employing higher resolution. Further, the first-order dynamic effects of non-constant radiative cooling can also be investigated using the current model—for example, varying the R parameter as a function of whether the grid point is cloudy ($q > q_s$) or not. While here we emphasise the possible direct applications to the study of moist convection as an alternative to CRMs and other more sophisticated

models, the current model by itself is of broad interest to researchers studying fundamental fluid dynamics and instabilities, chaos, turbulence, and dynamic systems in general. The system is particularly rich in transitions and dynamics, given that the dynamics of the system itself feeds back on to the energetics of the system—moisture provides a feedback between convection and energy as more convection leads to more latent heating, thus more buoyant forcing and convection. However, latent heating aloft also stabilises the system by increasing the temperature of the bulk and decreasing the effective Rayleigh number. We believe that such simplified approaches can help improve our fundamental understanding of the complex behaviour of moist convection.

ACKNOWLEDGEMENTS

The authors gratefully acknowledge the help of Julian Renaud and Alzbeta “Bety” Pechacova. Julian went through the relevant literature on the topic in the initial stages of the study in a very thorough manner and allowed the authors to understand the various types of idealised models that have been studied and the various approaches used. Bety ran simulations and performed analysis of the outputs of several simulations, which were crucial to bringing the article to its final form.

The authors also acknowledge the input of Prof. Martin Singh (Monash University, Australia) and discussions with Gregory Dritschel, Prof. Steven Tobias, and Prof. Douglas Parker (Leeds University, United Kingdom).

This project has received funding from the European Union’s Horizon 2020 research and innovation programme under the Marie Skłodowska-Curie grant agreement No. 101034413. C. Muller gratefully acknowledges funding from the European Research Council (ERC) under the European Union’s Horizon 2020 research and innovation program (Project CLUSTER, Grant Agreement No. 805041). This research was supported by the Scientific Service Units (SSU) of IST Austria through resources provided by Scientific Computing (SciComp).

CONFLICT OF INTEREST STATEMENT

The authors report no conflict of interest.

DATA AVAILABILITY STATEMENT

The data that support the findings of this study are available from the corresponding author, Lokhith Agasthya, upon reasonable request.

ENDNOTE

¹This excellent article can be found in pages 11–16 of the PDF document titled “Proceedings at the meetings of the society. January 19, 1938” from Volume 64, Issue 275, available for download from the online archives of the journal.

ORCID

Lokahith Agasthya  <https://orcid.org/0000-0001-8689-4540>

Caroline Muller  <https://orcid.org/0000-0001-5836-5350>

REFERENCES

- Agasthya, L. & Muller, C.J. (2024) Dynamics and scaling of internally cooled convection. *Communications in Nonlinear Science and Numerical Simulation*, 134, 108011.
- Ahlers, G., Grossmann, S. & Lohse, D. (2009) Heat transfer and large scale dynamics in turbulent rayleigh-bénard convection. *Reviews of Modern Physics*, 81, 503.
- Arakawa, A. & Schubert, W.H. (1974) Interaction of a cumulus cloud ensemble with the large-scale environment, part i. *Journal of the Atmospheric Sciences*, 31, 674–701.
- Arakawa, A. & Wu, C.-M. (2013) A unified representation of deep moist convection in numerical modeling of the atmosphere. Part i. *Journal of the Atmospheric Sciences*, 70, 1977–1992.
- Berlengiero, M., Emanuel, K., Von Hardenberg, J., Provenzale, A. & Spiegel, E. (2012) Internally cooled convection: a fillip for philip. *Communications in Nonlinear Science and Numerical Simulation*, 17, 1998–2007.
- Bjerknes, J. (1938) Saturated-adiabatic ascent of air through dry-adiabatically descending environment. *QJ Roy. Meteor. Soc.*, 64, 325–330.
- Bony, S. & Dufresne, J.-L. (2005) Marine boundary layer clouds at the heart of tropical cloud feedback uncertainties in climate models. *Geophysical Research Letters*, 32, L20806. Available from: <https://agupubs.onlinelibrary.wiley.com/doi/abs/10.1029/2005GL023851>
- Bouillaut, V., Lepot, S., Aumaitre, S. & Gallet, B. (2019) Transition to the ultimate regime in a radiatively driven convection experiment. *Journal of Fluid Mechanics*, 861, R5.
- Bretherton, C.S. & Smolarkiewicz, P.K. (1989) Gravity waves, compensating subsidence and detrainment around cumulus clouds. *Journal of Atmospheric Sciences*, 46, 740–759.
- Burns, K.J., Vasil, G.M., Oishi, J.S., Lecoanet, D. & Brown, B.P. (2020) Dedalus: a flexible framework for numerical simulations with spectral methods. *Physical Review Research*, 2, 023068.
- Davies, L., Jakob, C., May, P., Kumar, V. & Xie, S. (2013) Relationships between the large-scale atmosphere and the small-scale convective state for darwin, Australia. *Journal of Geophysical Research: Atmospheres*, 118, 11–534.
- Emanuel, K.A. (1994) *Atmospheric convection*. USA: Oxford University Press.
- Goluskin, D. (2015) Internally heated convection beneath a poor conductor. *Journal of Fluid Mechanics*, 771, 36–56.
- Goluskin, D. (2016) *Internally heated convection and Rayleigh-Bénard convection*. Cham, Switzerland: Springer International Publishing.
- Hernandez-Duenas, G., Majda, A.J., Smith, L.M. & Stechmann, S.N. (2013) Minimal models for precipitating turbulent convection. *Journal of Fluid Mechanics*, 717, 576–611.
- Holloway, C.E. & Neelin, J.D. (2009) Moisture vertical structure, column water vapor, and tropical deep convection. *Journal of the Atmospheric Sciences*, 66, 1665–1683.
- Jeevanjee, N. & Fueglistaler, S. (2020) Simple spectral models for atmospheric radiative cooling. *Journal of the Atmospheric Sciences*, 77, 479–497.
- Khairoutdinov, M.F. & Randall, D.A. (2003) Cloud resolving modeling of the arm summer 1997 iop: model formulation, results, uncertainties, and sensitivities. *Journal of the Atmospheric Sciences*, 60, 607–625.
- Klein, S.A., Hall, A., Norris, J.R. & Pincus, R. (2017) Low-cloud feedbacks from cloud-controlling factors: a review. *Surveys in Geophysics*, 38, 1307–1329.
- Manabe, S. & Strickler, R.F. (1964) Thermal equilibrium of the atmosphere with a convective adjustment. *Journal of the Atmospheric Sciences*, 21, 361–385.
- Muller, C.J., O’Gorman, P.A. & Back, L.E. (2011) Intensification of precipitation extremes with warming in a cloud-resolving model. *Journal of Climate*, 24, 2784–2800.
- Parodi, A. & Emanuel, K. (2009) A theory for buoyancy and velocity scales in deep moist convection. *Journal of the Atmospheric Sciences*, 66, 3449–3463.
- Pauluis, O. & Schumacher, J. (2010) Idealized moist rayleigh-bénard convection with piecewise linear equation of state. *Communications in Mathematical Sciences*, 8, 295–319.
- Robe, F.R. & Emanuel, K.A. (1996) Moist convective scaling: some inferences from three-dimensional cloud ensemble simulations. *Journal of Atmospheric Sciences*, 53, 3265–3275.
- Sherwood, S.C., Bony, S., Boucher, O., Bretherton, C., Forster, P.M., Gregory, J.M. et al. (2015) Adjustments in the forcing-feedback framework for understanding climate change. *Bulletin of the American Meteorological Society*, 96, 217–228 <https://journals.ametsoc.org/view/journals/bams/96/2/bams-d-13-00167.1.xml>
- Sherwood, S.C., Webb, M.J., Annan, J.D., Armour, K.C., Forster, P.M., Hargreaves, J.C. et al. (2020) An assessment of earth’s climate sensitivity using multiple lines of evidence. *Reviews of Geophysics*, 58, e2019RG000678. Available from: <https://agupubs.onlinelibrary.wiley.com/doi/abs/10.1029/2019RG000678>
- Shraiman, B.I. & Siggia, E.D. (1990) Heat transport in high-rayleigh-number convection. *Physical Review A*, 42, 3650.
- Shutts, G. & Gray, M. (1999) Numerical simulations of convective equilibrium under prescribed forcing. *Quarterly Journal of the Royal Meteorological Society*, 125, 2767–2787.
- Singh, M.S. & O’Gorman, P.A. (2013) Influence of entrainment on the thermal stratification in simulations of radiative-convective equilibrium. *Geophysical Research Letters*, 40, 4398–4403.
- Singh, M.S. & O’Gorman, P.A. (2014) Influence of microphysics on the scaling of precipitation extremes with temperature. *Geophysical Research Letters*, 41, 6037–6044 <https://agupubs.onlinelibrary.wiley.com/doi/abs/10.1002/2014GL061222>
- Singh, M.S. & O’Gorman, P.A. (2015) Increases in moist-convective updraught velocities with warming in radiative-convective equilibrium. *Quarterly Journal of the Royal Meteorological Society*, 141, 2828–2838 <https://rmets.onlinelibrary.wiley.com/doi/abs/10.1002/qj.2567>
- Sparrow, E.M., Goldstein, R.J. & Jonsson, V. (1964) Thermal instability in a horizontal fluid layer: effect of boundary conditions and non-linear temperature profile. *Journal of Fluid Mechanics*, 18, 513–528.
- Stauffer, C.L. & Wing, A.A. (2022) Properties, changes, and controls of deep-convecting clouds in radiative-convective equilibrium. *Journal of Advances in Modeling Earth Systems*, 14, e2021MS002917. Available from: <https://agupubs.onlinelibrary.wiley.com/doi/abs/10.1029/2021MS002917>

- Stevens, B., Satoh, M., Auger, L., Biercamp, J., Bretherton, C.S., Chen, X. et al. (2019) Dyamond: the dynamics of the atmospheric general circulation modeled on non-hydrostatic domains. *Progress in Earth and Planetary Science*, 6, 1–17.
- Tompkins, A.M. & Craig, G.C. (1998) Radiative–convective equilibrium in a three-dimensional cloud-ensemble model. *Quarterly Journal of the Royal Meteorological Society*, 124, 2073–2097.
- Vallis, G.K., Parker, D.J. & Tobias, S.M. (2019) A simple system for moist convection: the rainy–bénard model. *Journal of Fluid Mechanics*, 862, 162–199.
- van der Walt, S., Schönberger, J.L., Nunez-Iglesias, J., Boulogne, F., Warner, J.D., Yager, N. et al. (2014) Scikit-image: image processing in python. *PeerJ*, 2, e453. Available from: <https://doi.org/10.7717/peerj.453>
- Wing, A.A. & Emanuel, K.A. (2014) Physical mechanisms controlling self-aggregation of convection in idealized numerical modeling simulations. *Journal of Advances in Modeling Earth Systems*, 6, 59–74 <https://agupubs.onlinelibrary.wiley.com/doi/abs/10.1002/2013MS000269>
- Yano, J.-I. & Plant, R. (2012) Finite departure from convective quasi-equilibrium: periodic cycle and discharge–recharge mechanism. *Quarterly Journal of the Royal Meteorological Society*, 138, 626–637.
- Zelinka, M.D., Klein, S.A., Qin, Y. & Myers, T.A. (2022) Evaluating climate models' cloud feedbacks against expert judgment. *Journal of Geophysical Research: Atmospheres*, 127, e2021JD035198.

SUPPORTING INFORMATION

Additional supporting information can be found online in the Supporting Information section at the end of this article.

How to cite this article: Agasthya, L., Muller, C. & Cheve, M. (2025) Moist convective scaling: Insights from an idealised model. *Quarterly Journal of the Royal Meteorological Society*, 151:e4902. Available from: <https://doi.org/10.1002/qj.4902>

APPENDIX A. NON-DIMENSIONAL PARAMETERS

To non-dimensionalise the equations, we must define appropriate length, time, and temperature scales \mathcal{L} , t_0 , and \mathcal{T} respectively. Given that our equations are identical to (Vallis *et al.*, 2019) apart from the $-R$ term, any of the three routes of non-dimensionalisation suggested in their work (see their section 4.1, appendix A.1, and appendix A.2) could be applied directly. This would easily lead to a non-dimensionalised cooling rate given by Rt_0/\mathcal{T} .

However, as noted in the main text, the leading cause of instability and driver of convection in the current model is the radiative cooling. It would be more appropriate to non-dimensionalise the equations such that the applied

radiative cooling is of order unity as in previous works of internally forced convection (Agasthya & Muller, 2024; Berengiero *et al.*, 2012; Goluskin, 2015). We introduce temperature and time-scales \mathcal{T} and t_0 respectively, such that

$$R = \mathcal{T} t_0^{-1}. \quad (\text{A1})$$

Using q_0 as the specific humidity scale and the height of the domain L_z as the length scale, we set $t_0 = L_z^2/\kappa$ as the time-scale, which gives κ/L_z as the velocity scale. This is the usual diffusive scaling for velocity and it yields the following non-dimensionalised equations:

$$\nabla \cdot \mathbf{u} = 0, \quad (\text{A2})$$

$$\partial_t \mathbf{u} + (\mathbf{u} \cdot \nabla) \mathbf{u} = -\nabla p + \text{Pr} \nabla^2 \mathbf{u} + \text{Ra}_R T, \quad (\text{A3})$$

$$\partial_t T + \mathbf{u} \cdot \nabla T + N_1 w = \nabla^2 T + N_2 (q - q_s)_+ - 1, \quad (\text{A4})$$

$$\partial_t q + \mathbf{u} \cdot \nabla q = \text{Pr}_q \nabla^2 q - N_3 (q - q_s)_+, \quad (\text{A5})$$

where all state variables and operators are non-dimensionalised by their respective scales. The non-dimensional parameters are Ra_R , Pr , Pr_q , N_1 , N_2 and N_3 . These are given by

$$\text{Ra}_R = \frac{\beta g R L_z^5}{\nu \kappa^2}; \quad \text{Pr} = \frac{\nu}{\kappa}; \quad \text{Pr}_q = \frac{\kappa q}{\kappa}; \quad (\text{A6})$$

$$N_1 = \frac{\Gamma_d \kappa}{R L_z}; \quad N_2 = \frac{L_v q_0}{R \tau}; \quad N_3 = \frac{L_z^2}{\kappa \tau}. \quad (\text{A7})$$

Ra_R is a radiative Rayleigh number analogous to the buoyancy Rayleigh number and the condensation Rayleigh number of Val2019. The parameter N_1 is a non-dimensional dry-adiabatic lapse rate. Given that the condensation time-scale τ does not directly play a role in the dynamics, we foresee that it is the ratio of N_2 and N_3 given by $R L_z^2 / (q_0 \kappa L_v)$ that plays an important role in setting the dynamics of the system. Indeed, it is the ratio of the buoyancy effect due to heat release by condensation to the cooling by radiation, analogous to the parameter denoted $\hat{\gamma}$ in Val2019.

The system is driven by three different forcings—the thermal boundaries, the moisture boundaries, and the bulk cooling. Understanding the dependence of the static stability of the system on the various non-dimensional parameters and the scaling of the dynamics of the system in the convective regime as a function of these parameters remains outside the scope of the current study. The interested reader is encouraged to look at Sparrow *et al.* (1964), or within the references of Goluskin (2016), to understand the stability and dynamics of dry, internally cooled thermal fluid systems. Studies on the stability and dynamics of moist models of thermal convection are admittedly rarer.